International Journal of Heat and Mass Transfer 52 (2009) 1561–1572

Contents lists available at ScienceDirect

International Journal of Heat and Mass Transfer

journal homepage: www.elsevier.com/locate/ijhmt

A novel split-dimple interrupted fin configuration for heat transfer augmentation

Mohammad A. Elyyan, Danesh K. Tafti *

High Performance Computational Fluids-Thermal Sciences and Engineering Laboratory, Mechanical Engineering Department, Virginia Polytechnic Institute and State University, 114-I Randolph Hall, Blacksburg, VA 24061, USA

ARTICLE INFO

Article history:
Received 27 May 2008
Received in revised form 28 July 2008
Available online 10 October 2008

Keywords:
Heat enhancement
Fin
Split-dimple
Compact heat exchangers
LES

ABSTRACT

The use of an interrupted plate fin with surface roughness in the form of split-dimples is investigated. High-fidelity time-dependent calculations are performed for a wide range of Reynolds number ranging from $Re_H = 240$ to 4000, covering the laminar to fully turbulent flow regimes. The split-dimples provide an additional mechanism for augmenting heat transfer by perturbing continuous boundary layer formation on the fin surface and generating energetic shear layers. High heat transfer regions are observed at the fin and split-dimple leading edges as a result of boundary layer restarts, in regions of flow acceleration between protrusions, and flow impingement on the protrusion surface. While the protruding geometry of the split-dimple also aids in augmenting heat transfer from the fin surface by generating unsteady or turbulent wakes, it also increases pressure losses. The split-dimple fin results in a heat conductance that is 60–175% higher than a plain interrupted plate fin, but at a cost of 4–8 times the frictional losses.

1. Introduction

Air-side thermal resistance constitutes up to 80% of the total thermal resistance of heat exchangers. To improve the heat transfer capacity, fins are employed to increase the surface area as well as to increase the heat transfer coefficient. Fins, more often than not, use enhanced surfaces, which can broadly be classified into continuous fins with roughness or surface enhancements (e.g. wavy fins, dimpled fins)[1–5] or interrupted surfaces (e.g. offset strip, louvered, slit) [6–8]. Both surfaces are designed to disrupt the thermal boundary layer and increase mixing with the gas. At low Reynolds numbers typical of the laminar regime, surface interruptions are more effective than surface roughness in augmenting heat transfer.

Fig. 1 shows the heat transfer augmentation ratio of a 2D corrugated louvered fin (without tube effects) [7,9] compared to a continuous fin surface with dimples and protrusions as roughness elements [10]. Three typical louver geometries with varying louver angles are plotted versus two dimple geometries, which vary in dimple depth (characteristic roughness scale). Case 1 has a dimple depth of 0.2 times the channel height and Case 2 with dimple depth of 0.4. It is clear that in the low Reynolds number regime, louvered fins or more generally interrupted surfaces are far superior to the use of dimples and protrusions or more generally uninterrupted fins with roughness elements. In the example above, Case 1 with roughness depth less than the boundary layer thickness (half fin pitch for fully developed flow) shows no augmentation till the development of self-sustained flow oscillations at approximately $Re_H = 1000$. Case 2, which has a larger dimple depth of the same order as the boundary layer thickness, induces self-sustained oscillations in the flow much earlier and as a result is successful in augmenting the heat transfer coefficient. However, in spite of this, the augmentation in heat transfer coefficient is much lower than that in louvered fins. Louvered fins, in spite of operating in the laminar regime over most of the Reynolds number range in Fig. 1, result in high augmentation by constantly regenerating the thermal boundary layer at each louver.

Since interrupted surfaces are superior in augmenting heat transfer at low Reynolds numbers, this paper investigates the use of a hypothetical fin geometry which consists of an interrupted in-line fin surface combined with the dimple geometry. However, instead of using conventional dimples and protrusions, the dimple is split into two halves which are punched in opposite directions to produce what is called a split-dimple. The geometry is shown in Fig. 2. The objective of the paper is twofold: the first is to investigate the friction and heat transfer characteristics of the augmented geometry, and the second is to highlight the application of Large-Eddy Simulations (LES) to the complex geometrical configuration.

2. Governing equations and computational model

The computational model assumes the flow to be fully developed hydrodynamically and thermally to allow the simulation of a periodically repeating spatial unit. Heat is applied to the fin surfaces by using a constant heat flux (q''^*) boundary condition at the fin walls. A characteristic length taken as the fin pitch (H^*), a characteristic velocity taken as the friction velocity ($u_\tau^* =$

* Corresponding author.
E-mail address: dtafti@vt.edu (D.K. Tafti).
URL: http://www.hpcfd.me.vt.edu (D.K. Tafti).

0017-9310/$ - see front matter © 2008 Elsevier Ltd. All rights reserved.
doi:10.1016/j.ijheatmasstransfer.2008.07.046

Nomenclature

D	dimple imprint diameter
D_h	hydraulic diameter
C_f	Fanning friction coefficient
f	non-dimensional frequency based on mean velocity and fin pitch
g^{ij}	contravariant metric tensor
k	thermal conductivity
S	stream-wise pitch
H	channel height or fin pitch (characteristic length scale)
L_x	periodic length
$\vec{n}$	surface normal vector
Nu	Nusselt number
P	span-wise pitch
p	fluctuating, modified, or homogenized pressure
Pr	Prandtl number
q''	constant heat flux on channel walls
Q_x	flow rate in the stream-wise direction
Re_τ	Reynolds number based on friction velocity (u_τ)
Re_H	Reynolds number based on mean flow velocity (u_b) and H
t	non-dimensional time based on u_τ and H
Time	non-dimensional time based on u_b and H
$\vec{u}$	Cartesian velocity vector
u_τ	friction velocity (characteristic velocity)
u_b	mean flow velocity
$\vec{x}$	physical coordinates
β	mean pressure gradient
δ	dimple depth
γ	mean temperature gradient
θ	fluctuating, modified, or homogenized temperature
Ω	heat transfer surface area
$\vec{\xi}$	computational coordinates

Subscripts

b	bulk
D_h	based on the channel's hydraulic diameter
f	fin surface
H	based on channel height
o	smooth channel
t	turbulent parameters
τ	based on friction velocity

Superscripts

+	wall coordinates
*	dimensional quantities

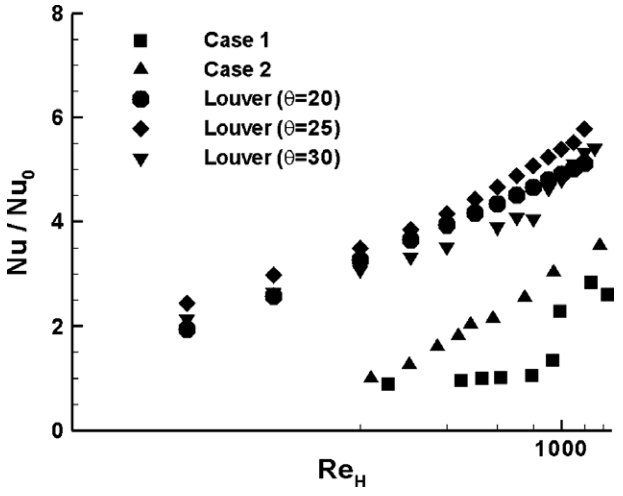

Fig. 1. Nusselt number augmentation for dimpled channel (Case 1 and Case 2) and typical louvered fin configuration.

$\sqrt{\tau^*_{w\,eq}/\rho^*}$), and a characteristic temperature given by q''^*H^*/k, are used to non-dimensionalize the Navier–Stokes and energy equations. Periodicity of the domain in the stream-wise (x) direction is accommodated by decomposing the stream-wise flow pressure and temperature into mean and fluctuating components. Pressure and temperature decomposition are given by

$$\begin{aligned} P^*(\vec{x},t) &= P^*_{in} - \beta^* x^* + p^*(\vec{x},t) \\ T^*(\vec{x},t) &= T^*_{in} + \gamma^* x^* + \theta^*(\vec{x},t) \end{aligned} \tag{1}$$

where β^* and γ^* are the mean gradients of pressure and temperature, respectively. On substitution into the flow and energy governing equations, the *non-dimensional* time-dependent equations in transformed coordinates $\vec{\xi} = \vec{\xi}(\vec{x})$ take the following conservative form[1]:

Continuity:

$$\frac{\partial}{\partial \xi_j}\left(\sqrt{g}U^j\right) = 0 \tag{2}$$

Momentum:

$$\begin{aligned} \frac{\partial}{\partial t}(\sqrt{g}u_i) + \frac{\partial}{\partial \xi_j}\left(\sqrt{g}U^j u_i\right) &= -\frac{\partial}{\partial \xi_j}(\sqrt{g}(\vec{a}^j)_i p) \\ &+ \frac{\partial}{\partial \xi_j}\left(\left(\frac{1}{Re_\tau} + \frac{1}{Re_{t_\tau}}\right)\sqrt{g}g^{jk}\frac{\partial u_i}{\partial \xi_k}\right) \\ &+ \sqrt{g}\beta\delta_{i1} \end{aligned} \tag{3}$$

Energy:

$$\begin{aligned} \frac{\partial}{\partial t}(\sqrt{g}\theta) + \frac{\partial}{\partial \xi_j}\left(\sqrt{g}U^j\theta\right) &= \frac{\partial}{\partial \xi_j}\left(\left(\frac{1}{PrRe_\tau} + \frac{1}{Pr_t Re_{t_\tau}}\right)\sqrt{g}g^{jk}\frac{\partial \theta}{\partial \xi_k}\right) \\ &- \sqrt{g}\gamma u_1 \end{aligned} \tag{4}$$

where $\vec{a}^i$ are the contravariant basis vectors,[2] $\sqrt{g}$ is the Jacobian of the transformation, g^{ij} are the elements of the contravariant metric tensor, $\sqrt{g}U^j = \sqrt{g}(\vec{a}^j)_i u_i$ is the contravariant flux vector, $\vec{u}_i$ is the Cartesian velocity vector, and θ is the modified temperature. The non-dimensional mean pressure and temperature gradients are found from mean momentum and energy balances, respectively, as

$$\begin{aligned} \beta &= \frac{4}{D_h} \\ \gamma &= \frac{\Omega}{Re_\tau Pr Q_x L_x} \end{aligned} \tag{5}$$

More details about the modified fully developed treatment can be found in Zhang et al. [11].

Re_{t_τ} is the inverse of the non-dimensional turbulent eddy-viscosity and it is modeled by the Smagorinsky model as

[1] Henceforth, all usage is in terms of non-dimensionalized values.

[2] The notation $(\vec{a}^j)_k$ is used to denote the kth component of vector $\vec{a}^j$. $(\vec{a}^j)_k = \partial \xi_j / \partial x_k$.

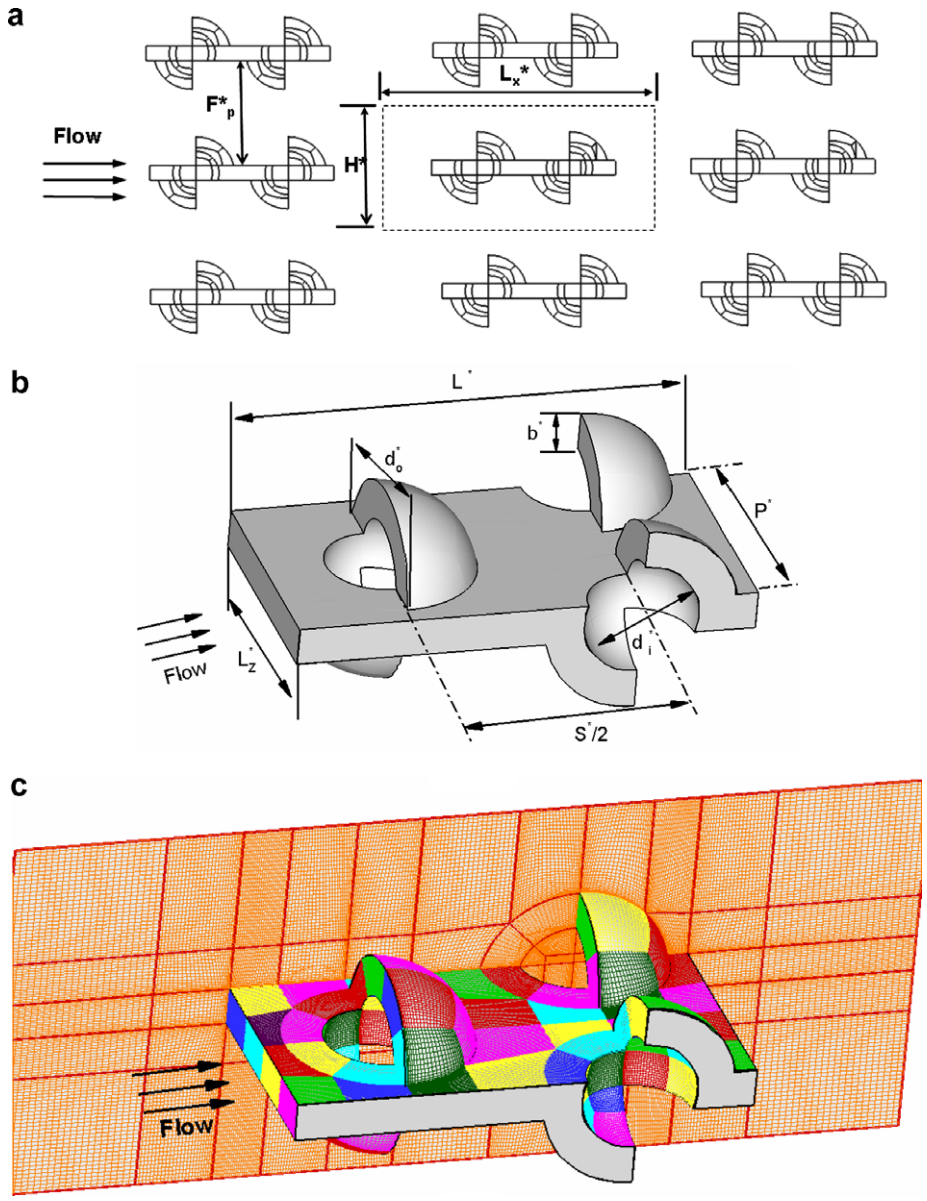

Fig. 2. Split-dimple fin: (a) arrangement; (b) geometry; (c) domain mesh.

$$\frac{1}{Re_{t_\tau}} = C_s^2(\sqrt{g})^{2/3}|\bar{S}| \tag{6}$$

where $|\bar{S}|$ is the magnitude of the resolved strain rate tensor given by $|\bar{S}| = \sqrt{2\bar{S}_{ik}\bar{S}_{ik}}$. The Smagorinsky constant (C_s^2) is obtained via the dynamic subgrid stress model [12]. The turbulent Prandtl number is assumed to have a constant value of 0.5 [13].

A conservative finite-volume formulation using a second-order central difference scheme on a non-staggered grid topology is used to discretize the governing equations. In this scheme, the flow velocity and scalar variables are calculated and stored at the cell center, whereas the contravariant fluxes are calculated and stored at the cell faces. Temporal advancement is performed using a two-step projection method. An intermediate velocity field is calculated at the predictor step, which is then updated at the corrector step by satisfying discrete continuity.

The computer program GenIDLEST (Generalized Incompressible Direct and Large-Eddy Simulations of Turbulence) is used for the current study. GenIDLEST has been applied extensively to air-side heat transfer augmentation calculations and validated with experimental results in the literature, e.g. Cui and Tafti [14], Sewall et al. [15] and Elyyan et al. [10]. Details about the algorithm, functionality, and capabilities can be found in Tafti [16].

3. Calculation of friction and heat transfer coefficients

Low pressure drop and high heat transfer rate are the goals of any new fin shape design, and in order to quantify these characteristics the Fanning friction coefficient and Nusselt number are used to evaluate the performance of the split-dimple fin. The Fanning friction coefficient is calculated as

$$C_f = \frac{\tau_s^*}{\rho^*(u_b^*)^2/2} = \frac{-(\Delta\overline{p}_x^*/L_x^*)D_h^*}{2\rho^*(u_b^*)^2} \tag{7}$$

where D_h^* is the dimensional hydraulic diameter of the fin. Non-dimensionalizing with the corresponding characteristic length and velocity and substituting for the mean pressure gradient from Eq. (5) result in

$$C_f = \frac{D_h}{2u_b^2} \tag{8}$$

The fin surface heat transfer is characterized by a surface averaged Nusselt number, Nu, which is calculated as

$$Nu = \frac{h^* H^*}{k^*} = \frac{q''^* H^* \Omega_f^*}{k^* \int (T_s^* - T_{ref}^*) d\Omega_f^*} \tag{9}$$

where h^* is the average convective heat transfer coefficient of the surface, k^* is the thermal conductivity, q''^* is the wall heat flux, T_s^* is the fin surface temperature, and T_{ref}^* is a reference temperature, respectively. Non-dimensionalizing with the corresponding characteristic length and temperature scales the Nusselt number can be rewritten as

$$Nu_{avg} = \frac{\Omega_f}{\int\int (\theta_s - \theta_{ref}) d\Omega_f} \tag{10}$$

where θ_s and θ_{ref} are the local modified non-dimensional fin surface and reference temperatures, respectively. The reference temperature is the volume-averaged temperature of the domain found by integrating the heat flux over the entire volume

$$\theta_{ref} = \frac{\int\int\int |u| \theta dA_x dx}{\int\int\int |u| dA_x dx} \tag{11}$$

4. Baseline friction and heat transfer coefficients

The performance of the new fin geometry is evaluated by comparing its friction coefficient and Nusselt number to that of a smooth parallel-plate channel. The laminar friction coefficient and Nusselt number for a smooth parallel-plate channel with fin pitch (H^*) are given by

$$C_{f_0} = 12/Re_H; \quad Re_H < 1500 \tag{12}$$

$$Nu_0 = 4.12; \quad Re_H < 1500 \tag{13}$$

and for the turbulent regime, the Peutokhov and Gnielinski correlations for the friction coefficient and Nusselt number, respectively, are used [17]

$$C_{f_0} = (1.580 \ln Re_H - 2.185)^{-2}; \quad 1500 \leqslant Re_H \leqslant 2.5 \times 10^6 \tag{14}$$

$$Nu_0 = \frac{(C_{f_0}/2)(Re_H - 500)Pr}{1 + 12.7(C_{f_0}/2)^{1/2}(Pr^{2/3} - 1)}; \quad 1500 \leqslant Re_H \leqslant 2.5 \times 10^6 \tag{15}$$

Note that the hydraulic diameter for a smooth parallel-plate channel is equal to twice the fin pitch ($D_h^* = 2H^*$), i.e. ($Re_{D_h} = 2Re_H$). Thus, the original Peutokhov and Gnielinski correlations are rewritten here in terms of Re_H rather than Re_{D_h}.

5. Fin geometry, computational domain, and grid independency

The fin geometry is composed of a parallel inline fin array, which is assumed to be infinite in the span-wise direction. Two rows of split-dimples modify the fin surface as shown in Fig. 2. Fig. 2b shows the fin's smallest repeatable spatial unit that can be used to represent the fin geometry; this spatial unit is used in the current study. The computational domain is assumed to be periodic in the span-wise, stream-wise, and transverse directions. Table 1 summarizes the computational domain's geometry specifications – non-dimensionalized by the fin pitch ($F_p^* = H^*$).

A grid independency study is conducted for the split-dimple fin geometry; where three grid resolutions have been tested. All of the grid cases used 288 structured/unstructured grid blocks to represent the fin geometry, Fig. 2c. In order to resolve the near wall turbulence at the fin surface, a fine mesh resolution is placed in the vicinity of the surface. The same grid distribution was used in the direction normal to the fin surface for all three cases. While the finest grid consisted of 3.6 million cells, the next level was constructed by coarsening in the span-wise direction to 1.93 million cells, and the coarsest level of 1.16 million cells was obtained by coarsening both the span-wise and stream-wise directions. All grid cases are tested at a nominal Reynolds number of 4000, which is the highest Reynolds number considered in this paper. Calculations are started with an initial guess for the velocity and temperature fields in the domain and allowed to develop in time under the specified pressure drop until the flow is fully developed and stationary, after which temporal averaging for mean and turbulent quantities is initiated.

Table 1
Split-dimple fin geometry specifications

Fin geometry specifications				
Fin pitch H	Domain length L_x	Fin length L	Fin thickness b	
1.0	2.4	1.2	0.1	
Split-dimple specifications				
Dimple outer diameter d_o	Dimple inner diameter d_i	Dimple stream-wise pitch S	Dimple span-wise pitch P	Dimple depth δ
0.5	0.3	1.2	0.6	0.15

Table 2
Grid independency test results

Case	No. of cells	Re_H	C_f	% Diff	Nu_{avg}	Max % diff
1	1.16E+06	4022	0.283	0.55	69.6	1.22
2	1.93E+06	4033	0.281	1.10	70.4	0.10
3	3.58E+06	4011	0.284	Ref.	70.4	Ref.

Table 2 summarizes the friction coefficient and surface averaged Nusselt number values for the split-dimple fin for the three grids, with Case 3 – the finest mesh case – taken as a reference for comparison. It is found that the difference in the friction coefficient and Nusselt number for the three grid cases is less than 1.5%. In spite of this, due to the complexity of the fin shape and the desire to perform a very accurate analysis of the flow structures, turbulent statistics, and heat transfer distribution in the domain, the finest grid of 3.6 million cells is used for all the calculations.

In addition to the grid independency study, the sufficiency of the 3.6 million resolution was further verified by checking the y^+ distribution obtained through an *a-posteriori* calculation of the local friction velocity at the highest Reynolds number simulated in this study ($Re_H = 4000$). Fig. 3 shows the y_1^+ distribution of the first grid point normal to the wall surface at the top and bottom sides of the fin. The distribution shows that the condition of $y_1^+ < 1$ is satisfied for most of the fin surface except for small regions at the bottom where the maximum y_1^+ value is 4.9. This guarantees the existence of at least one point inside the laminar sublayer of the flow. The wall parallel mesh distribution maintains a maximum value of $\Delta_{//}^+ = 40$ at the highest Reynolds number simulated.

In order to evaluate the performance of the split-dimple fin, numerical simulations of a smooth plate fin are conducted. The dimensions and boundary conditions of the plate fin are selected to match those of the split-dimple fin with fin pitch of 1, fin length of 1.2, fin thickness of 0.1, and domain length of 2.4. Two computational domains are used in the calculations: (i) a 2D domain constructed using 10 mesh blocks and 46,080 cells used for low Reynolds number flows ($Re_H < 1400$); (ii) a 3D domain constructed with 20 grid blocks and 442,368 cells applied for higher Reynolds number flows ($Re_H > 1400$).

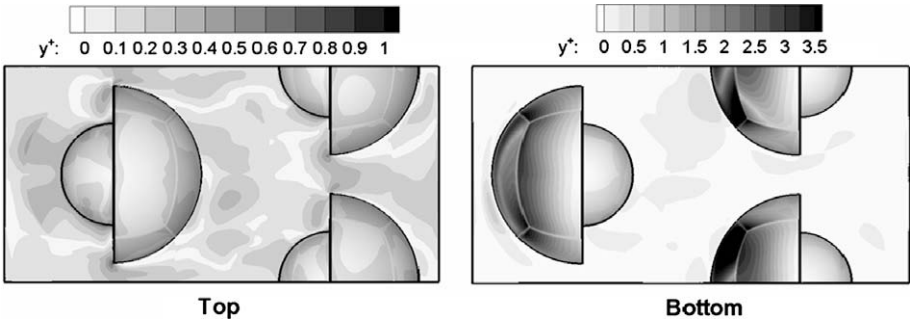

Fig. 3. y^+ distribution at the top and bottom fin surfaces of the split-dimple fin at $Re_H = 4000$.

6. Results and discussion

Numerical simulations of the split-dimple fin covered a wide range of Reynolds number flows, $Re_H = 250–4000$, ranging from laminar to fully turbulent flows. Calculations are initiated with an initial guess for the velocity and temperature fields in the domain, and the flow is then allowed to develop with time under the prescribed pressure gradient. At a stage when the velocity or flow rate exhibits a stationary signal, which is constant for steady flow or one with a constant mean value for unsteady flows, temporal averaging is activated to obtain time-mean quantities for unsteady flows. The typical averaging time ranges between 2.5 and 6 time units or between 2 and 5 domain flows through time units. The plate fin calculations covered a Reynolds number range of $Re_H = 300–3700$.

6.1. Instantaneous flow structure

Fig. 4 shows the time-history of the stream-wise velocity at $Re_H = 360$, 460, 570, and 1100 at three locations: near the protrusion at the fin's top surface, inside the dimple cavity, and near the protrusion's surface at the fin's bottom side. The velocity signals at $Re_H = 360$ show close to steady laminar flow with some very low amplitude oscillations for the selected locations. These low

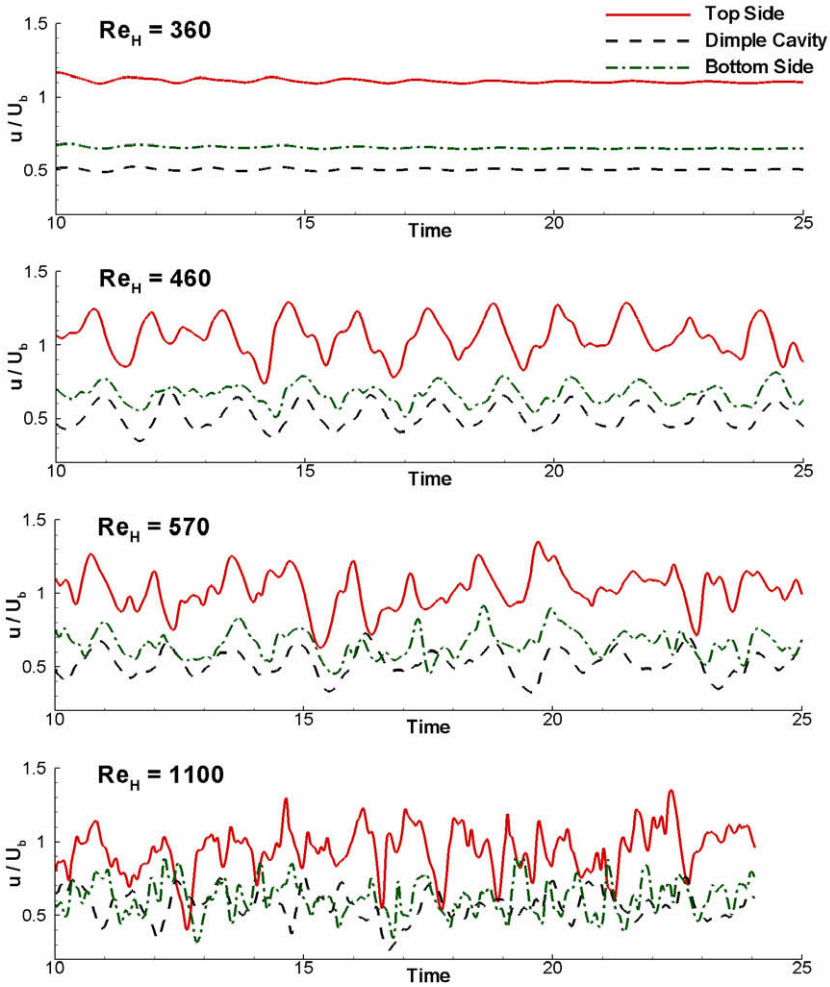

Fig. 4. Split-dimple's instantaneous stream-wise velocity signals normalized with the bulk velocity for $Re_H = 360$, 460, 570 and 1100.

amplitude oscillations are suspected to be remnants from the higher Re_H run from which the calculation was initiated. For all practical purposes, the flow at $Re_H = 360$ is steady. At $Re_H = 460$, the flow shows signs of unsteady flow with a dominant non-dimensional frequency (fU_b/H) of 0.72. As the Reynolds number increases to $Re_H = 570$ and 1100, the range of frequencies increase as secondary instabilities develop and the flow becomes chaotic and eventually turbulent. In comparison, the plate fin shows low amplitude periodic oscillations at $Re_H = 330$ signifying the developing instability in the leading edge shear layer at a fundamental non-dimensional frequency of 0.34. These oscillations keep growing till they become chaotic at $Re_H = 1330$, as seen in Fig. 5.

Fig. 6 shows the educed coherent-vorticity at $Re_H = 1100$ (level = 25) and 4000 (level = 50) on the fin's top and bottom sides.

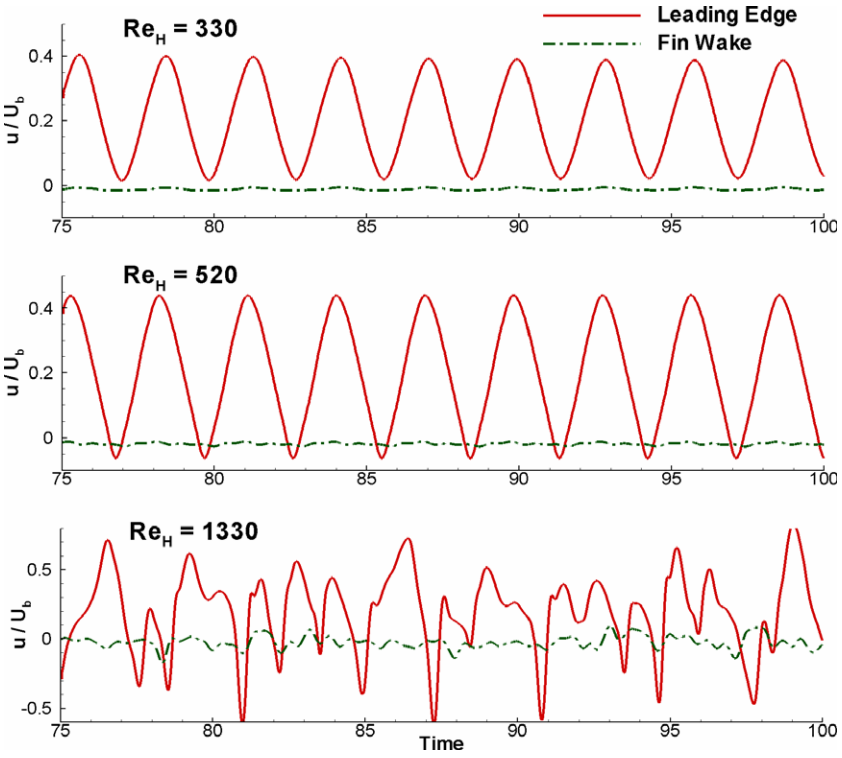

Fig. 5. Plate fin's instantaneous stream-wise velocity signals normalized with bulk velocity for $Re_H = 330$, 520 and 1330.

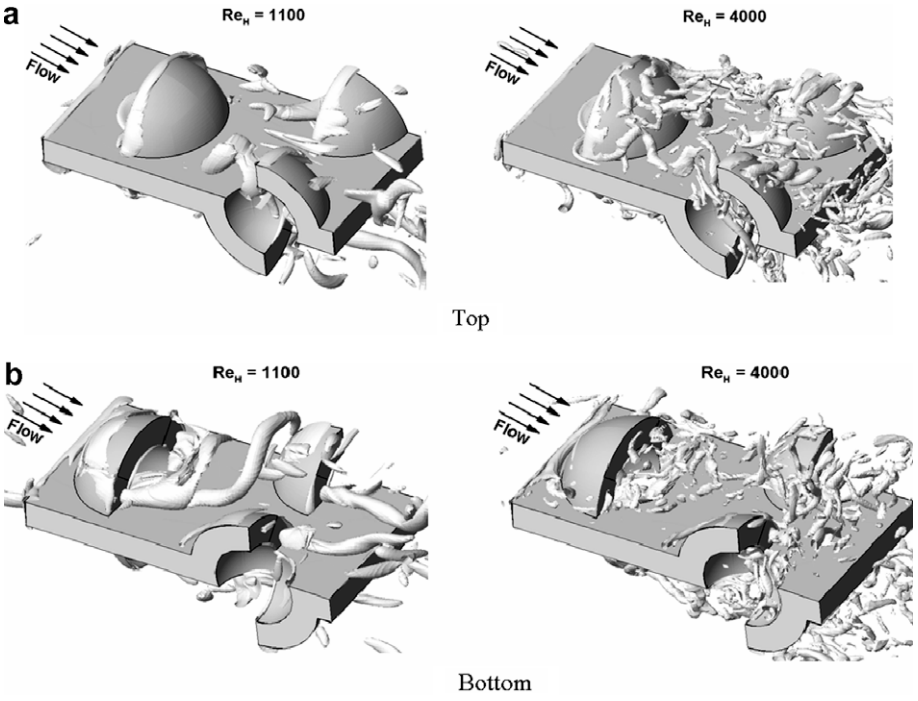

Fig. 6. Isosurfaces of coherent-vorticity for the split-dimple fin for $Re_H = 1100$ (left), isosurface level = 25, and 4000 (right), isosurface level = 50, on the (a) top side; (b) bottom side.

The coherent-vorticity is identified by the vortex-eduction technique proposed by Chong et al. [18]. Roller or span-wise aligned vortices are shed from the fin's leading edge and the leading edge of the protrusion on the fin's top surface. The shed vortices convect downstream, where some of them impinge at the downstream protrusion's inner surface and are redirected to the fin's bottom side through the split-dimple opening. On the fin's bottom surface, once again roller vortices are shed from the leading edge of the fin. These roller vortices are deformed by the flow accelerating around the protrusion and form a horseshoe like vortex at the leading edge of the protrusion. There is considerable vorticity ejected out of the split-dimple opening. At the lower $Re_H = 1100$, the ejected vortices take an elongated hairpin like shape, which degenerates to small scale vorticity (turbulence) at $Re_H = 4000$.

6.2. Mean flow structure

Fig. 7 shows three-dimensional mean flow features by injecting mean velocity streamlines close to the fin's top (left) and bottom (right) surfaces at $Re_H = 240$, 1100 and 4000, covering laminar to fully turbulent regimes.

Fig. 8 plots the streamlines in a 2D stream-wise plane ($z = 0$). Several important flow features which influence heat transfer are present in the domain

- Large flow recirculation zone in the wake of the protrusion at the fin's top side. As the Reynolds number increases, the reattachment length of the wake decreases due to higher flow momentum and turbulence.
- Recirculation region inside the dimple cavity on the fin's top side as the flow separates at the upstream edge of the dimple at $Re_H = 1100$ and 4000. As the Reynolds number increases from $Re_H = 1100$–4000, the recirculation zone's size shrinks. A much smaller recirculation zone is observed for the laminar flow at $Re_H = 240$.
- Flow impingement at the protrusion's front surface on the fin's bottom side, and at the inner protrusion's surface on the fin's top side.

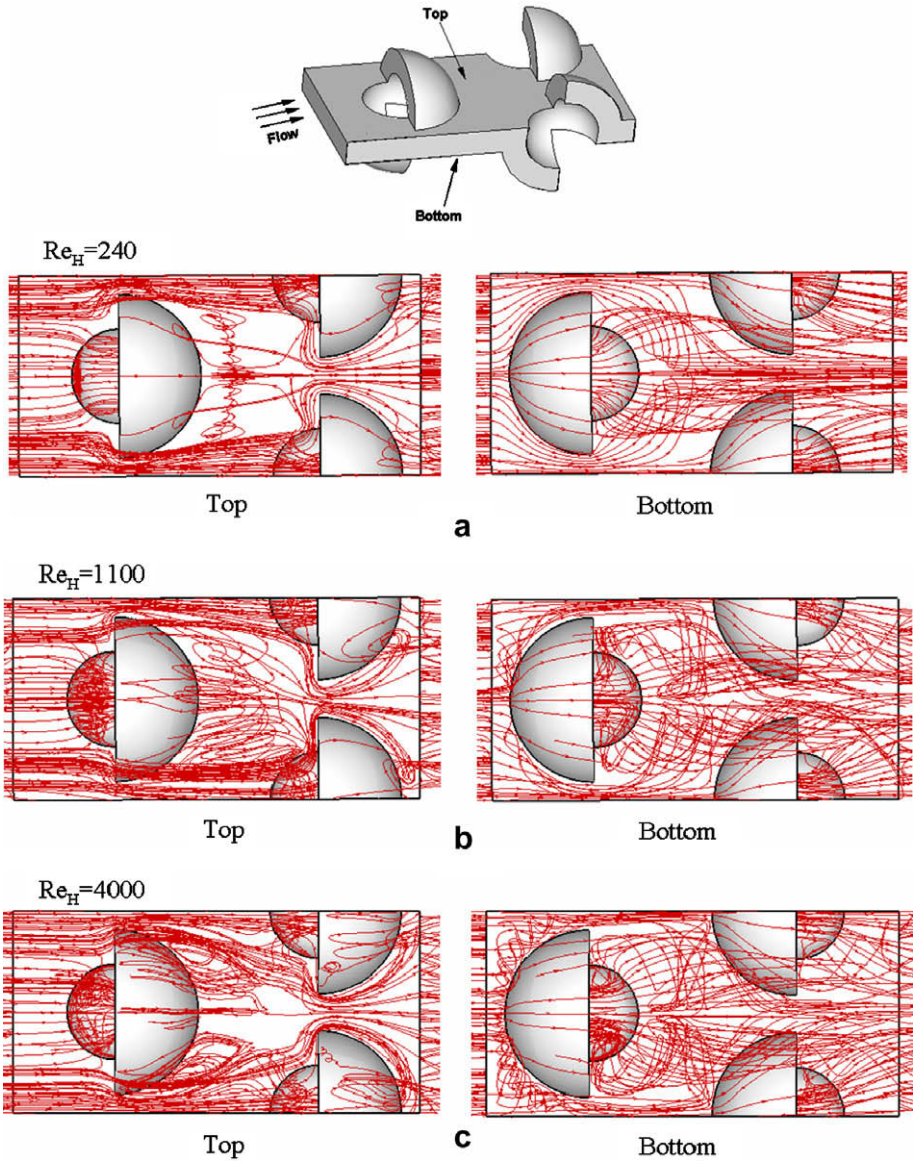

Fig. 7. Mean velocity stream lines at top (left) and bottom (right) sides of fin at Re_H = (a) 240; (b) 1100; (c) 4000. (Flow from left to right.)

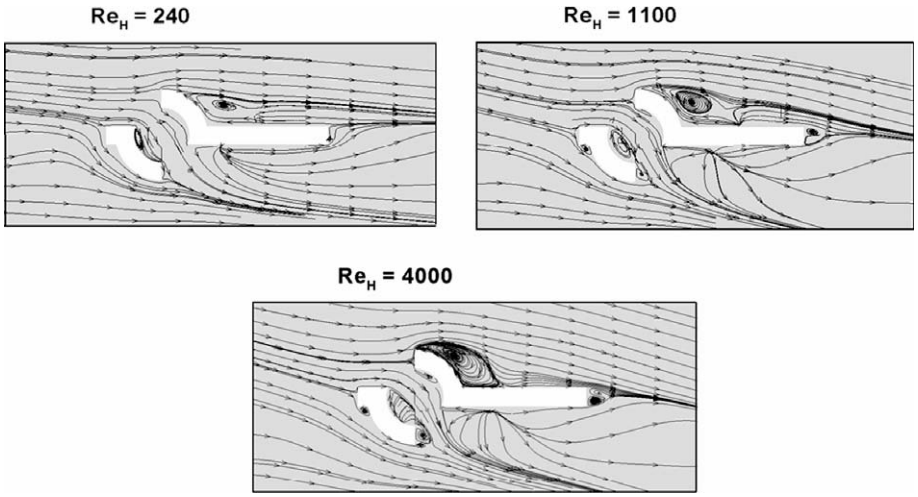

Fig. 8. Mean velocity streamlines at a stream-wise plane crossing the center of the domain ($Z = 0$) for $Re_H = 240$, 1100 and 4000.

- A swirling jet issuing from the split-dimple cavity as seen at the fin's bottom side. The flow redirection from the fin's top side to its bottom side through the dimple cavity results from the low pressure in the wake of the protrusion at the bottom. Swirl is imparted to the flow by the curved edges of the dimple cavity. Due to the partial blocking of the dimple cavity by the recirculating flow inside it, the redirected flow through the split-dimple opening eject in an-almost normal direction to the main flow. Upon exiting the split-dimple opening, the redirected flow is partially realigned by the mainstream flow. Due to the larger blocking and faster redirected flow as the Reynolds number increases, flow realignment becomes weaker.
- A horseshoe type vortex is observed at the upstream rim of the protrusion on the bottom side of the fin for $Re_H = 1100$ and 4000. This horseshoe vortex is formed by the separated shear layer from the fin's leading edge, which accelerates and elongates around the protrusion's surface. The 3D horseshoe vortex is seen in Fig. 6 and as a small recirculating region in Fig. 7.
- Flow acceleration through the narrow passage between protrusions at the fin's top and bottom sides.

6.3. Turbulent statistics

Turbulent kinetic energy (TKE) levels give a good indication of the heat transfer rate from the fin's surface, where high TKE values indicate strong flow mixing and high heat transfer, and vice versa. Fig. 9 shows the TKE distribution, normalized by the mean bulk velocity squared, for the fully turbulent flow at $Re_H = 4000$ at stream-wise locations starting from the downstream edge of the dimple cavity, x = − 0.15, to the next dimple cavity's downstream

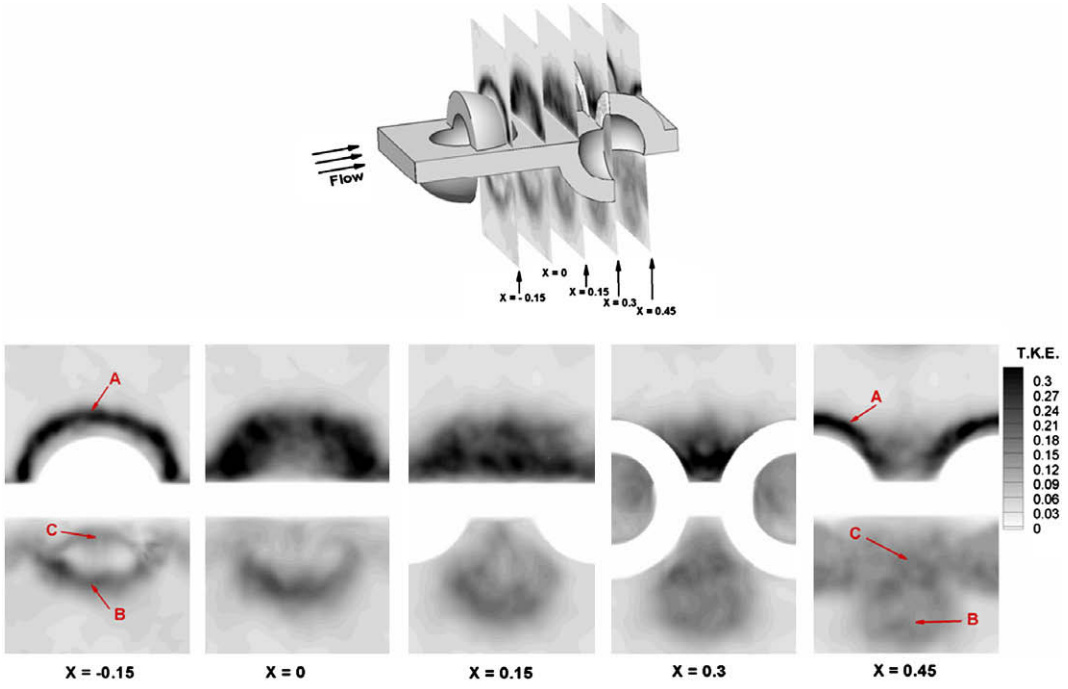

Fig. 9. Normalized TKE distribution at selected stream-wise locations in the split-dimple fin at $Re_H = 4000$.

edge, $x = 0.45$. The main sources of turbulent kinetic energy production are the separated shear layers, which form at the leading (labeled A in Fig. 8) and trailing edges of the protrusion (labeled B) on the fin's top and bottom sides, respectively, and through the shear imparted to the jet issuing from the dimple cavity (labeled C). While the TKE produced in A stays close to the surface of the fin due to reattachment, the TKE in B and C is transported away from the fin surface.

Fig. 10 shows the normalized TKE profile at selected stream-wise locations along the fin's centerline ($z = 0$) for the flow at $Re_H = 1100$, 2000 and 4000. The TKE profiles peak at the flow separation from the protrusion's surface on the fin's top surface, $x = -0.15$ (A in Fig. 8). This peak occurs at almost the same y-location for the three flows ($y = 0.3$), and the highest value occurs for the fully turbulent flow of $Re_H = 4000$. As the flow moves downstream, the TKE peak diffuses towards the fin surface. Note that

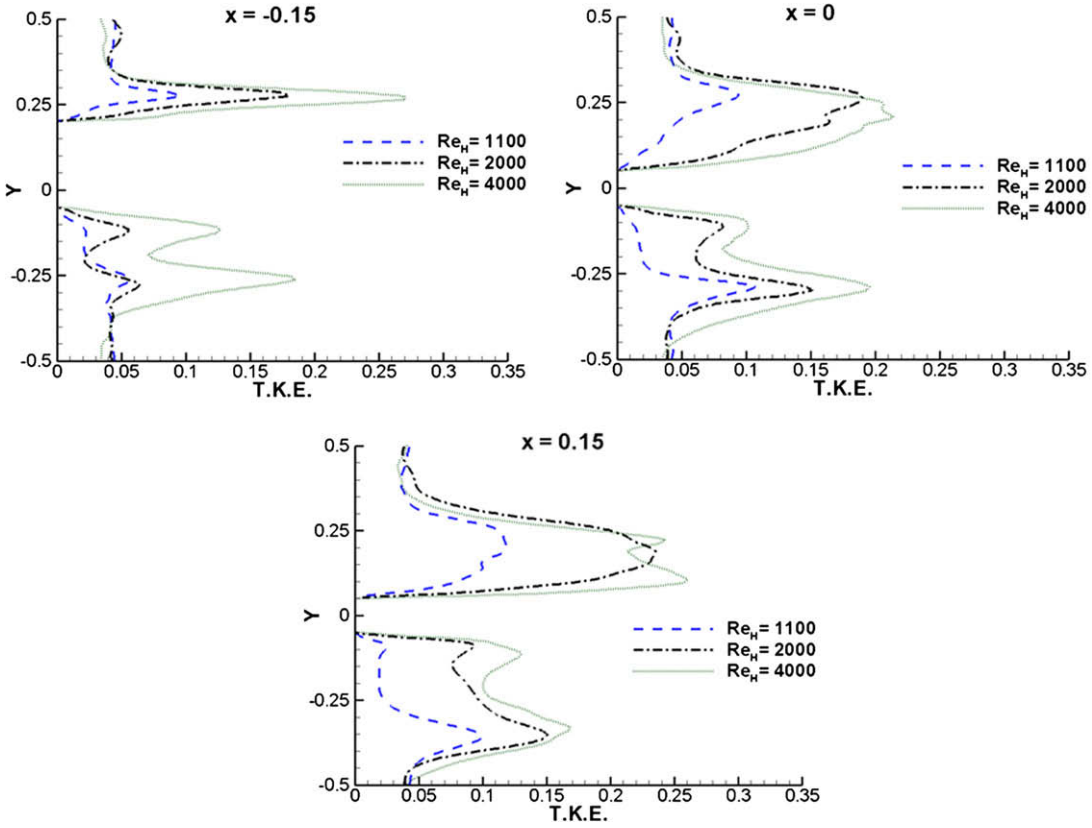

Fig. 10. Normalized TKE profile for the flow at $Re_H = 1100$, 2000 and 4000 at selected stream-wise locations across the center line of the fin ($z = 0$).

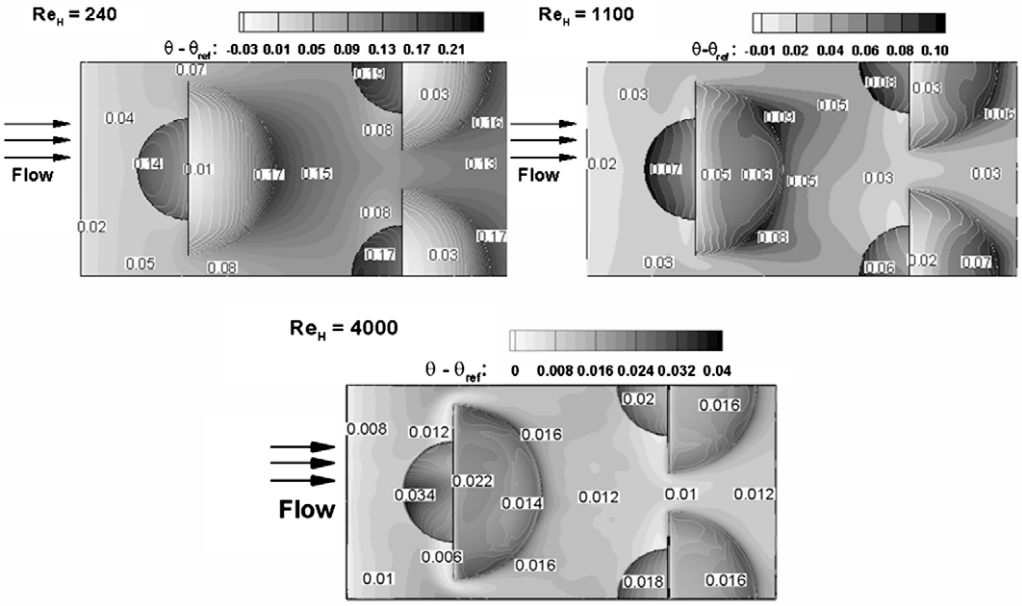

Fig. 11. Heat transfer distribution at the top fin surface represented by $(\theta - \theta_{ref})$ for $Re_H = 240$, 1100 and 4000.

the TKE levels at $Re_H = 2000$ approach those at $Re_H = 4000$ in the flow reattachment region downstream of the protrusion, ($x = 0$, and 0.15). The maximum TKE ranges between 20% and 30% at $Re_H = 4000$.

On the bottom side of the fin, dual peaks appear at the split-dimple opening for the fully turbulent flows at $Re_H = 2000$ and 4000, while a single rather weak peak exists for the flow at $Re_H = 1100$. The dual peaks result from the shear imparted to the flow exiting the split-dimple cavity (C) and the interaction of the outer flow and flow issuing from the cavity (B). These peaks convect downstream of the split-dimple's opening ($x = 0$, and 0.3), where they diffuse and move away from the fin's surface.

6.4. Heat transfer distribution

Heat transfer augmentation results from the disruption of the thermal boundary layer, flow impingement, and flow instabilities or turbulence. Boundary layer regeneration is the dominant mechanism at low Reynolds numbers, which is augmented by flow instabilities as the Reynolds number increases. The temperature difference $(\theta_s - \theta_{ref})$ is an indicator of the local variation in heat transfer coefficient as given by Eq. (9), where low values indicate regions of high heat transfer coefficients, and larger values occur in regions of low heat transfer coefficients.

Figs. 11 and 12 show $(\theta_s - \theta_{ref})$ distribution on the top and bottom fin surfaces, respectively, for the flow at $Re_H = 240$, 1100 and 4000. Regions of high heat transfer, small $(\theta_s - \theta_{ref})$, exist at (i) boundary layer regeneration at the leading edge of the fin, leading edge of the protrusion on the top surface, and downstream of dimple on the bottom surface, (ii) velocity acceleration zone in the narrow passage between protrusions – especially at high Reynolds numbers, (iii) flow impingement region at the protrusion's outer and inner faces, (iv) flow reattachment region in the wake of the protrusion on the top surface, and (v) the junction eddy at the protrusion's leading edge at the fin's bottom surface for the turbulent flows at $Re_H = 1100$ and 4000.

Conversely, regions of low heat transfer, large $(\theta_s - \theta_{ref})$, exist at (i) flow recirculation region inside the dimple cavity and downstream of the protrusion, and (ii) in the wake of the split-dimple opening at the fin's bottom side. Note that the size of the high $(\theta_s - \theta_{ref})$ zone in the wake of the protrusion shrinks with increasing Reynolds number of the flow, and it is almost unnoticeable at the fully turbulent flow case at $Re_H = 4000$. This agrees with the

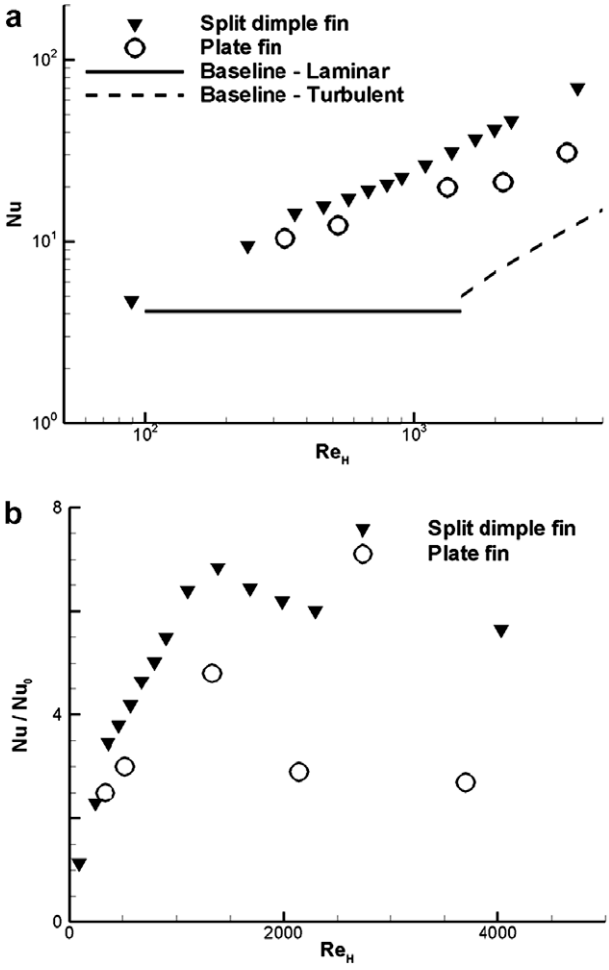

Fig. 13. Comparison of the Nusselt number and Nusselt number ratio for the split-dimple fin and flat plate fin: (a) Nu; (b) Nu/Nu_0.

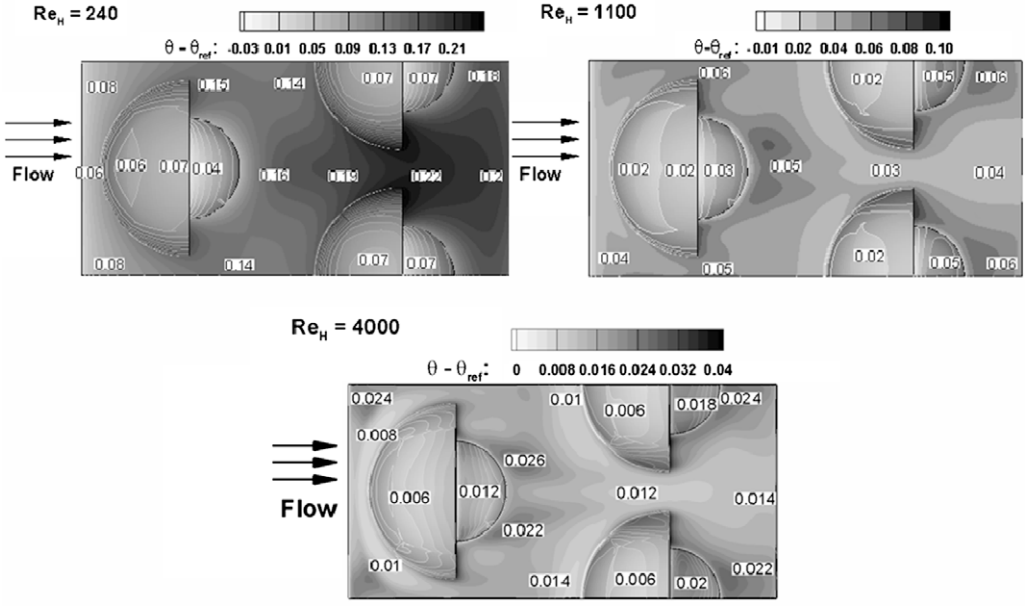

Fig. 12. Heat transfer distribution at the bottom fin surface represented by $(\theta - \theta_{ref})$ for $Re_H = 240$, 1100 and 4000.

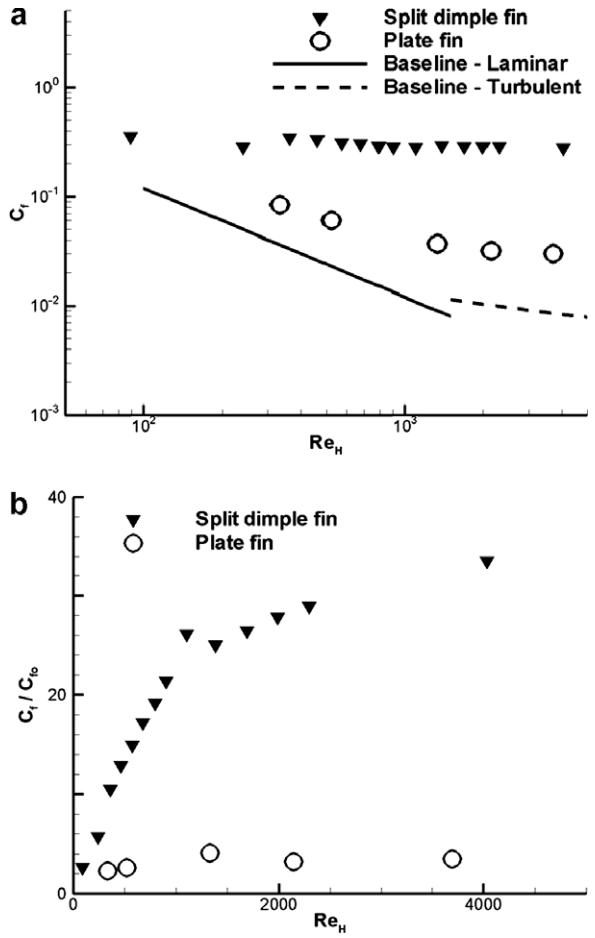

Fig. 14. Comparison of the friction coefficient and friction coefficient ratio for the split-dimple and flat plate fin: (a) C_f; (b) C_f/C_{fo}.

early flow reattachment observed earlier for the fully turbulent flows, Figs. 7c and 8 ($Re_H = 4000$). In general, as the Reynolds number increases, the $(\theta_s - \theta_{ref})$ range becomes smaller and more uniform in distribution, which indicates strong flow mixing for turbulent flows.

6.5. Average friction and heat transfer coefficient

Fig. 13 shows the Nusselt number and its augmentation for the split-dimple and plate fin. Better heat transfer performance is obtained with the split-dimple fin over the plate fin with 40–120% increase of Nusselt number. Moreover, the split-dimple fin has a heat transfer area that is 45% larger than the plate fin, which results in an additional increase of split-dimple fin heat conductance ($h\Omega$). Thus, the conductance is increased between 60% and 175% over the plate fin.

Fig. 14 shows the friction coefficient and its augmentation ratio compared to a plain channel flow for both the split-dimple and plate fins. As expected, the split-dimple fin produces much larger pressure drop than the plate fin; where the extra protuberances introduced into the flow by the split-dimple fin geometry produce a significant increase in flow resistance. The split-dimple fin's friction coefficient is 4–8 times that of the plate fin.

7. Summary and conclusions

Time-dependent high-fidelity calculations have been conducted for a hypothetical fin shape, combining an interrupted plate fin with surface roughness in the form of split-dimples covering a wide range of Reynolds numbers $Re_H = 250–4000$. Detailed investigation of the transient and fully turbulent flow structures, turbulent statistics, and heat transfer distribution showed the following major flow and thermal features:

- The split-dimple geometry augments the overall effectiveness of the interrupted fin by disrupting the thermal boundary layer which forms on the fin surface.
- Shear layers induced by the split-dimple geometry enhance turbulence levels in the flow and heat transfer from the fin surface. TKE levels as high as 30% are observed in the vicinity of the split-dimple.
- The windward surfaces of the split-dimple also contribute to heat transfer augmentation through the mechanism of flow impingement. High heat transfer is also observed at the flow acceleration zone between protrusions.
- Flow separation and large wakes are induced by the protruding split-dimple geometry, which reduce heat transfer and increase pressure losses in the flow. The fin surface downstream of the protrusion on both sides, and the surface inside the dimple cavity are examples of these regions. As the Reynolds number increases, these regions become smaller due to enhanced mixing.
- Overall, the split-dimple fin has 60–175% higher heat transfer capacity than the plate fins, but with 4–8 times the frictional losses.

Future work should focus on modifications for reducing the friction penalty.

Acknowledgments

This work is a result of support provided by the US Army RDECOM, Fort Belvoir, VA and Modine Manufacturing Co., Passenger Thermal Management, Racine, WI for air-side heat transfer enhancement in next generation compact heat exchangers. The support is gratefully acknowledged. The calculations were performed on Virginia Tech's Advanced Research Computing facility, System-X.

References

[1] C.C. Wang, W.L. Fu, C.T. Chang, Heat transfer and friction characteristics of wavy fin-and-tube heat exchangers, Exp. Thermal Fluid Sci. 14 (1998) 174–186.
[2] D. Junqi, C. Jiangping, C. Zhijiu, Z. Yimin, Z. Wenfeng, Heat transfer and pressure drop correlations for the wavy fin and flat tube heat exchangers, Appl. Thermal Eng. 27 (2007) 2066–2073.
[3] P.M. Ligrani, J.L. Harrison, G.I. Mahmood, M.L. Hill, Flow structure due to dimple depressions on a channel surface, Phys. Fluids 13 (11) (2001) 3442–3451.
[4] H.K. Moon, T.O. O'Connell, R. Sharma, Heat transfer enhancement using a convex-patterned surface, J. Turbomach. 125 (2003) 274–280.
[5] N.K. Burgess, M.M. Oliveira, P.M. Ligrani, Nusselt number behavior on deep dimpled surfaces within a channel, J. Heat Transfer 125 (2003) 11–18.
[6] J. Dong, J. Chen, Z. Chen, Y. Zhou, Air-side thermal hydraulic performance of offset strip fin aluminum heat exchangers, Appl. Thermal Eng. 27 (2007) 306–313.
[7] D.K. Tafti, L.W. Zhang, G. Wang, Geometry effects on flow transition in multilouvered fins – onset, propagation, and characteristics of frequencies, Int. J. Heat Mass 44 (2001) 4195–4210.
[8] C.C. Wang, W.H. Tao, C.J. Chang, An investigation of the airside performance of the slit fin-and-tube heat exchangers, Int. J. Refrig. 22 (1999) 595–603.
[9] X. Zhang, D.K. Tafti, Classification and effects of thermal wakes on heat transfer in multilouvered fins, Int. J. Heat Mass Transfer 44 (2001) 2461–2473.
[10] M.A. Elyyan, A. Rozati, D.K. Tafti, Investigation of dimpled fins for heat transfer enhancement in compact heat exchangers, Int. J. Heat Mass Transfer 51 (2008) 2950–2966.
[11] L. Zhang, D. Tafti, F. Najjar, S. Balachander, Computations of flow and heat transfer in parallel-plate fin heat exchangers on the CM-5: effects of flow

unsteadiness and three-dimensionality, Int. J. Heat Mass Transfer 40 (66) (1997) 1325–1341.
[12] M. Germano, U. Piomelli, P. Moin, W.H. Cabot, A dynamic subgrid-scale eddy viscosity model, Phys. Fluids 3 (1991) 1760–1765.
[13] P. Moin, K. Squires, W. Cabot, S. Lee, A dynamic sub-grid-scale model for compressible turbulence and scalar transport, Phys. Fluids A 3 (11) (1991) 2746–2757.
[14] J. Cui, D.K. Tafti, Computations of flow and heat transfer in a three-dimensional multilouvered fin geometry, Int. J. Heat Mass Transfer 45 (2002) 5007–5023.
[15] E.A. Sewall, D.K. Tafti, A.B. Graham, K.A. Thole, Experimental validation of large eddy simulation of flow and heat transfer in a stationary ribbed duct, Int. J. Heat Fluid Flow 27 (2) (2006) 243–258.
[16] D.K. Tafti, GenIDLEST – a scalable parallel computational tool for simulating complex turbulent flows, Proc. ASME Fluids Eng. Division FED 256 (2001) 346–357.
[17] F. Incropera, D. Dewitt, Fundamentals of Heat and Mass Transfer, fifth ed., Wiley, New York, 2001. pp. 463–493.
[18] M. Chong, A. Perry, B.J. Cantwell, A general classification of three-dimensional flow fields, Phys. Fluids A 2 (1990) 765–777.